Achieving high-density states through shock-wave loading of precompressed samples

Raymond Jeanloz*†‡, Peter M. Celliers§, Gilbert W. Collins§, Jon H. Eggert§, Kanani K. M. Lee¶, R. Stewart McWilliams*, Stéphanie Brygoo‖, and Paul Loubeyre‖

Departments of *Earth and Planetary Science and †Astronomy, University of California, Berkeley, CA 94720; §Lawrence Livermore National Laboratory, Livermore, CA 94550; ¶Department of Physics, New Mexico State University, Las Cruces, NM 88003; and ‖Commissariat à l'Energie Atomique, 91680 Bruyères-le-Châtel, France

Edited by Ho-kwang Mao, Carnegie Institution of Washington, Washington, DC, and accepted March 7, 2007 (received for review September 19, 2006)

Materials can be experimentally characterized to terapascal pressures by sending a laser-induced shock wave through a sample that is precompressed inside a diamond-anvil cell. This combination of static and dynamic compression methods has been experimentally demonstrated and ultimately provides access to the 10- to 100-TPa (0.1–1 Gbar) pressure range that is relevant to planetary science, testing first-principles theories of condensed matter, and experimentally studying a new regime of chemical bonding.

high pressure | planetary interiors | diamond-anvil cell | Hugoniot | laser shock

In nature, and specifically when considering planets, high pressures are clearly evident in two contexts: the conditions occurring deep inside large planetary bodies and the transient stresses caused by hypervelocity impact among planetary materials. In both cases, typical peak stresses are much larger than the crushing strength of minerals (up to ≈1–10 GPa, depending on material, strain rate, pressure, and temperature), so pressures can be evaluated by disregarding strength and treating the rock, metal, or ice as a fluid. Ignoring the effects of compression, the central (hydrostatic) pressure of a planet is therefore expected to scale roughly as the square of the planet's bulk density (ρ_{planet}, assumed constant throughout the planet) and radius (R_{planet}):

$$P_{center} \sim 7\ \mathrm{TPa}(\rho_{planet}/\rho_{Jupiter})^2(R_{planet}/R_{Jupiter})^2. \qquad [1]$$

Here, the scaling factor is adjusted to match the central pressure of Jupiter-like planets ($R_{Jupiter}$ and $\rho_{Jupiter}$ are the radius and bulk density of Jupiter, respectively), and the effects of compression and differentiation (segregation of dense materials toward the center of a planet) act to increase the central pressure for larger, denser, more compressed, or more differentiated planets relative to Eq. **1**. Consequently, peak pressures in the 1- to 10-TPa range exist inside large planets, with Earth's central pressure being 0.37 TPa and "supergiant" planets expected to have central pressures in the 10- to 100-TPa range.

In addition to static considerations, impact (the key process associated with growth of planets and the initial heating that drives the geological evolution of planets) is also expected to generate TPa pressures. Impedance-matching considerations described below can be combined with Kepler's third law to deduce that peak impact pressures for planetary objects orbiting a star of mass M_{star} at an orbital distance R_{orbit} are of the order

$$P_{impact} \approx 1\ \mathrm{TPa}(M_{star}/M_{Sun})(\rho_{planet}/5.5\ \mathrm{g\ cm^{-3}}) \cdot (R_{orbit}/1\ \mathrm{AU})^{-1}. \qquad [2]$$

Scaling here is to the mass of the Sun, and the average density and orbit of Earth, the latter being in astronomical units (1 AU = 1.496×10^{11} m); also, the characteristic impact velocity (u_0) is taken as the average orbital velocity according to Kepler's law, $u_0 = 2\pi R_{orbit}/T_{orbit}$ with T_{orbit} being the orbital period, and Eq. **2** assumes a symmetric hypervelocity impact.

While recognizing that materials have been characterized at such conditions through specialized experiments (e.g., shock-wave measurements to the 10- to 100-TPa range in the proximity of underground nuclear explosions and from impact of a foil driven by hohlraum-emitted x-rays) (1–3), laboratory experiments tend to achieve significantly lower pressures. As with planetary phenomena, both static (diamond-anvil cell) and dynamic (shock-wave) methods are available for studying macroscopic samples at high pressures, but these are normally limited to the 0.1- to 1-TPa range (4). Still, these pressures are of fundamental interest because the internal-energy change associated with compression to the 0.1-TPa (1 Mbar) level is roughly (5)

$$\Delta E \approx -P\Delta V \sim 10^5\ \text{joules per mole of atoms} \qquad [3]$$

with volume changes (ΔV) being ≈20% of the 5-cm^3 typical molar volume of terrestrial-planet matter (here we consider a mole of atoms, or gram-formula weight, which is 3.5, 5, and 6 cm^3 for diamond, MgO, and water, respectively, at ambient conditions). The work of compression thus corresponds to bonding energies (≈1 eV = 97 kJ per mole, characteristic of the outer, bonding electrons of atoms), meaning that the chemical bond is profoundly changed by pressures of 0.1 TPa. This expectation has been verified through numerous experiments showing that the chemical properties of matter are significantly altered under pressure: for instance, hydrogen, oxygen, and the "noble gas" xenon transform from insulating, transparent gas, fluids, or crystals at low pressure to become metals by ≈0.1 TPa (5, 6).

In this article, we briefly describe laboratory techniques that have recently been developed for studying materials to the 10- to 100-TPa range of relevance to planetary science. In particular, as most planets now known are supergiants of several (≈1.5–8) Jupiter masses orbiting stars at distances of a fraction of 1 astronomical unit (7), Eqs. **1** and **2** imply a strong motivation for characterizing materials up to the 100-TPa (1 Gbar) level. To reach such conditions, we combine static and dynamic techniques for compressing samples: specifically, propagating a shock wave through a sample that has been precompressed in a diamond-anvil cell (Fig. 1). By starting with a material that is already at high (static) pressures, one reaches higher compressions than could be obtained by driving a shock directly into an uncompressed sample.

Moreover, by varying the initial density (pressure) of the sample, and also by pulse-shaping the shock-wave entering the sample, one can tune the final pressure-density-temperature (P–ρ–T) state that is achieved upon dynamic loading. This tuning is particularly

Author contributions: R.J., G.W.C., and P.L. designed research; R.J., P.M.C., G.W.C., J.H.E., K.K.M.L., R.S.M., and S.B. performed research; P.M.C., G.W.C., J.H.E., K.K.M.L., S.B., and P.L. analyzed data; and R.J. wrote the paper.

The authors declare no conflict of interest.

This article is a PNAS Direct Submission.

Abbreviation: VISAR, velocity interferometry from the surface of any reflector.

‡To whom correspondence should be addressed. E-mail: jeanloz@uclink.berkeley.edu.

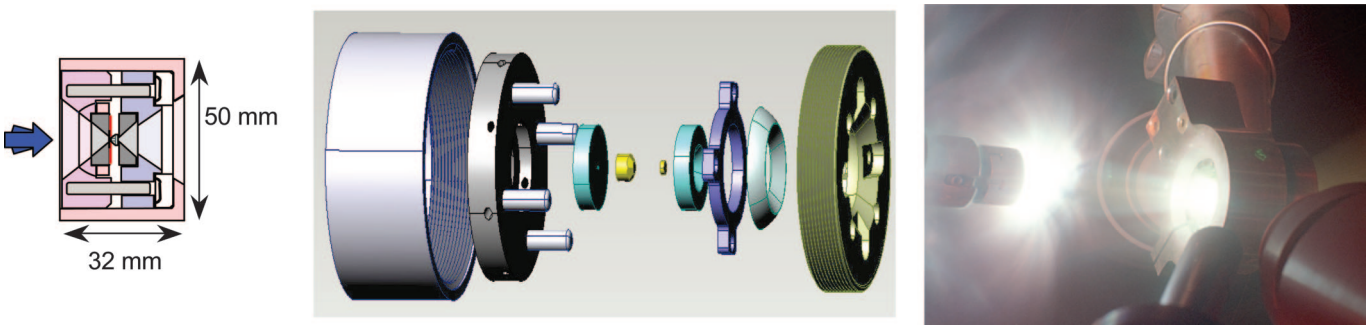

Fig. 1. Schematic of diamond-anvil cell (*Left* and *Center*), showing both a cross-section (blue arrow indicates direction of incoming, shock-wave generating laser beams) and a pulled-apart view, and photograph (*Right*) of a diamond cell as a laser-induced shock is being generated during an experiment at the Omega laser facility (University of Rochester, Rochester, NY).

relevant to planetary applications, because the average temperature profile through the convective interior of a planet is isentropic, rather than following a shock-compression curve (Hugoniot). Precompression thus allows one to significantly reduce the heating that tends to dominate the highest-pressure dynamic experiments, which is important for better characterizing the interatomic forces under compression.

Experimental Approach

Diamond-cell samples are necessarily small, ≈100–500 μm in diameter by 5–50 μm in thickness, as it is the small area of the diamond tip (culet) that allows high pressures to be achieved. Shock compression of such small samples is not well suited to experiments involving mechanical impact, for example, by a projectile launched from a light-gas gun (which currently sets the state of the art for high-quality shock-wave measurements, but involves sample dimensions of centimeter diameter by millimeter thickness). Instead, a laser-generated shock wave is better suited to the dimensions of the diamond cell, with a well defined shock front of ≈200–500 μm diameter being readily achieved at presently available facilities.

Several laser beams are typically focused onto the outer surface of one of the diamond anvils, so as to generate an intense pulse of light that is absorbed at the diamond surface (thin layers of laser-absorbing plastic and x-ray-absorbing Au usually are deposited on that diamond surface) (Fig. 2). The outermost diamond is thereby vaporized, launching a high-amplitude pressure wave into the anvil caused by a combination of the rapid thermal pressure

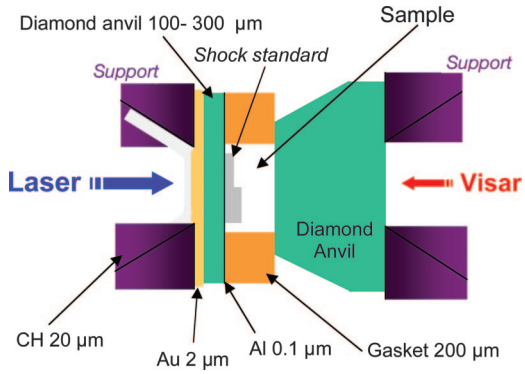

Fig. 2. Schematic cross-section of diamond anvils and sample, with the drive laser that creates the shock wave entering from the left. Supports for the anvils are shown in purple, and, as described in the text, current laser systems require the anvil on the shock-entry side to be thin. The sample is indicated, along with a stepped shock-wave standard, and diagnostics described in the text [VISAR and pyrometry (not shown)] record the dynamic compression of the sample through the second anvil.

generated in the diamond (resulting from heating at nearly constant volume) and linear-momentum balance ("rocket effect") relative to the diamond vapor that expands outward, back toward the incoming laser beams. Such a high-amplitude wave has the property of being self-steepening for a material with a normal equation of state ($\partial K_S/\partial P > 0$ for the adiabatic bulk modulus K_S). As a result, a shock front is created inside the anvil and propagates toward the sample (8, 9).

The sample itself is precompressed inside a metal gasket, either directly (e.g., if it is a fluid) or else within a pressure-transmitting fluid (Fig. 2). Current methods allow samples to be precompressed up to no more than ≈1–5 GPa, because the diamond anvil from which the shock front enters needs to be thin, no more than ≈100–400 μm thick (10, 11). This anvil amounts to little more than a microscope-slide coverslip, albeit made of diamond. As discussed below, this limitation arises from the short duration of laser pulses available at present-day facilities.

Two types of calibrants are included in the gasket hole, along with the sample: one or more small (≈1–10 μm) chips of ruby and a shock-wave standard. The ruby is used to measure the pressure of the precompressed sample (P_1), using the ruby-fluorescence method (12), from which the density of the sample (ρ_1) is determined before shock compression (the equation of state of the sample must therefore be known at the precompression pressures). The shock-wave standard consists of a metal plate, stepped so as to have at least two well determined thicknesses, or of a well characterized dielectric material that transforms to a metal under shock loading. In either case, the mechanical response of the shock-wave standard needs to be well known: i.e., to have a well determined relationship between shock and particle velocities, U_S and u_p, as well as the release or reshock response from the initial shock state. Aluminum, platinum, and tungsten are examples of shock-wave standards, and a measurement of the shock velocity (the shock-wave transit-times across the different, well calibrated thicknesses of the standard) then yields the particle velocity of the shock front entering into the sample (3, 13).

Upon exiting the first diamond anvil, the shock front traverses the sample chamber (including both sample and calibrants) and then transits through the second (back) diamond anvil. At this point, there is no concern if the shock wave decays, so the back anvil can be of typical thickness for high-pressure experiments (≈2.5 mm); it serves as a window, containing the sample and allowing its characterization during shock compression. Both anvils and the sample (and calibrants) are normally vaporized during an experiment, although the cell that contains the anvils is reuseable. With shock velocities of order ≈20 km/s = 20 μm/ns, the entire experiment is completed within a few nanoseconds.

A set of forward- and backward-traveling stress waves (shock or rarefaction) is in general created at each interface between diamond, calibrant, and sample, so a complete temporal record is

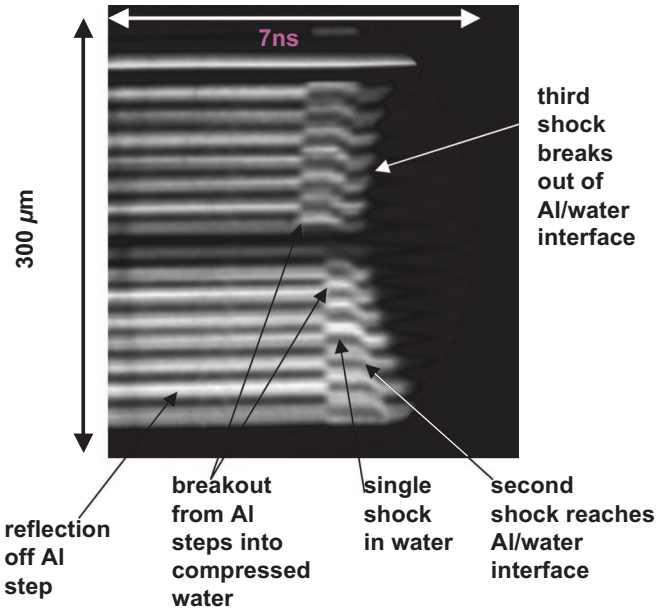

Fig. 3. VISAR record from a laser-shock experiment through a precompressed sample (14), showing velocity fringes as a function of time (horizontal axis) obtained from an optical streak camera imaging light reflected off the stepped-Al shock standard across the ≈300-μm width of the sample area (vertical axis). Fringe positions are proportional to velocity of the reflecting surface, so shifts in fringes (e.g., at breakout) indicate changes in velocity. Curvature in breakout times indicate that the shock fronts are not exactly planar, and the stepped breakout at the center of the image shows the difference in travel time through the thin and thick Al steps (Fig. 2).

needed of the various waves that traverse the sample. This record is usually obtained by velocity interferometry from the surface of any reflector (VISAR) (15), that provides a record of the shock and material (particle) velocities inside the sample chamber (Fig. 3). Briefly, VISAR operates by illuminating the sample with a single-frequency laser and imaging the reflected light through an interferometer onto a detector. The interferometer is configured to have unequal paths: a change in the frequency of the light passing through it causes a change in the fringe phase in proportion to the Doppler shift in frequency. The velocity of moving reflectors in the target (interfaces and shock fronts) are thereby measured to ≈1% precision. If the initial thickness of the (precompressed) sample is known, a measurement of the shock-wave transit time determines the shock velocity.

The pressure (P_H), density (ρ_H), and internal energy change ($E_H - E_1$) of the sample during shock compression are then determined by the Hugoniot relations that describe conservation of mass, linear momentum, and energy ($V = 1/\rho$ is specific volume) (8):

$$\rho_1 U_S = \rho_H (U_S - u_p) \quad [4]$$

$$P_H - P_1 = \rho_1 U_S u_p \quad [5]$$

$$E_H - E_1 = (1/2)(P_H + P_1)(V_1 - V_H). \quad [6]$$

Here, subscripts H and 1 indicate the shock-compressed (Hugoniot) state and the initial, unshocked (in the present case, statically precompressed) state, respectively; U_S is the velocity of the shock front (assumed to be steady), and u_p is the particle velocity to which the material is accelerated upon shock loading (without loss of generality, the material is taken as having $u_p = 0$ before shock compression). These relations describe a 1D compression such that, for unit cross-section, U_S and $\rho_1 U_S$ define a volume and corresponding mass of unshocked material that is

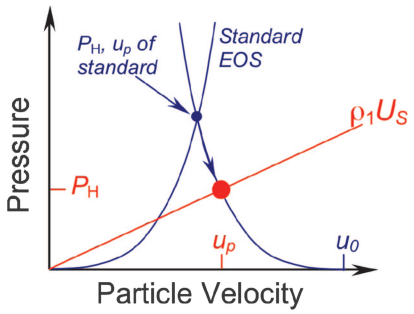

Fig. 4. Impedance matching solution for the Hugoniot pressure (P_H) and particle velocity (u_p) in the sample, as determined from the shock velocity U_S measured across the sample that by Eq. **5** defines the slope of the red line (P_1 is ignored here). The intersection with the equation of state of the standard (blue curve), reflected about the pressure–particle velocity state achieved in the standard (blue point), defines the common state (red point) behind the forward- and backward-traveling waves in the sample and standard. In a mechanical-impact experiment, u_0 would correspond to the impact velocity of the standard into the sample.

engulfed by the shock front in unit time. That mass is compressed to a volume $U_S - u_p$ having a density ρ_H; the volume change (per unit cross-section and mass transited by the shock front in unit time) is thus given by $-u_p$ in Eq. **4**. The pressure change across the shock front is the force per unit area (of cross-section), or the mass $\rho_1 U_S$ times the acceleration u_p in Eq. **5**. Finally, Eq. **6** states that (ignoring the precompression pressure P_1) half the $-P\Delta V$ compressional energy change is lost in accelerating the material to the velocity u_p on shock loading, and (combining with Eqs. **4** and **5**) the Hugoniot energy is proportional to u_p^2 (the internal energy is expressed here in J/kg = $m^2 \cdot s^{-2}$).

It is empirically found that the shock-wave velocity scales linearly with particle velocity for a wide variety of materials over a moderate range of compressions (8, 13, 16, 17):

$$U_S = c + s u_p. \quad [7]$$

The mass engulfed by the shock front per unit time, $\rho_1 U_S$, is therefore proportional to u_p, and the energy flux deposited into the sample then scales as $\approx u_p^3$ (energy per unit time and cross-sectional area). For a laser-produced shock wave, assuming the energy flux into the sample is proportional to the laser intensity I, at least for a moderate range of intensities, one consequently expects the shock pressure to scale roughly as

$$P \sim I^{2/3}. \quad [8]$$

In reality, laser-induced shock pressures appear to rise less rapidly than Eq. **8**, the exponent being closer to 0.6 than 0.7, no doubt because of inefficiencies in laser-target coupling that can become worse as I increases (18, 19) and to U_S ultimately increasing sublinearly with u_p [deviations from Eq. **7** typically involve a negative contribution quadratic in u_p (e.g., ref. 3), and the occurrence of phase transitions under shock compression likewise reduces U_S at a given u_p].

Although reasonable for understanding the conditions achieved by laser-driven shock waves, Eq. **8** is inadequate for determining the properties, notably, the equation of state, of a sample at high pressures. Instead, one applies the fact that conservation of mass and momentum require that both the particle velocity and pressure be constant across each interface traversed by the shock wave(s) (8, 16). Measuring the shock velocity, hence pressure, density, and particle velocity in the stepped shock-wave standard (blue point in Fig. 4), determines the magnitude of the stress wave about to enter the sample itself. The material velocity and pressure of the sample and standard

are brought to the common values u_p and P_H across the interface (red point in Fig. 4): the pressure in the standard decreases or increases, respectively, depending on whether it is less or more compressible than the sample (Fig. 4 illustrates the former case, with the pressure drop in the standard indicated by the curved blue arrow; in detail, a correction is made to account for the fact that the decompression follows an isentrope rather than the Hugoniot).

Conditions Achieved

To evaluate the conditions generated in laser-shock experiments on precompressed samples, we calculate the Hugoniot equation of state by way of the Mie–Grüneisen approach that takes the sample pressure (Hugoniot pressure P_H achieved on shock loading) as arising from two terms, compression along a reference path to the final volume (V) plus thermal pressure at that (constant) volume (16, 17):

$$P_H(V) = P_S(V) + (\gamma/V)[E_H(V) - E_S(V)]. \quad [9]$$

Here, the reference path is an isentrope, indicated by subscript S, and the Grüneisen parameter $\gamma = V(\partial P/\partial E)_V$ depends on volume and temperature (or thermal energy): as described below, ionization and other effects cause γ to depend on temperature.

The internal energy along the isentrope, $E_S(V)$, is given by the isentropic equation of state $P_S(V)$ because $-(\partial E/\partial V)_S = P_S$. We specifically use the Eulerian finite-strain formulation for the isentrope, motivated by the fact that the Cauchy stress (the trace of which gives the pressure) is intrinsically a function of Eulerian strain (20), and that the resulting equation of state is empirically found to successfully match experimental measurements involving both finite and infinitesimal compression (e.g., wave-velocity measurements) (17, 21). That is, the internal energy change upon isentropic compression is assumed well described by a Taylor expansion in the Eulerian finite-strain measure $f = (1/2)\,[(V/V_0)^{-2/3} - 1]$ (defined positive on compression)

$$\Delta E_S = (9/2)V_0K_{0S}f^2[1 + (K'_{0S} - 4)f + \ldots]. \quad [10]$$

K is the bulk modulus, subscript 0 indicates zero-pressure conditions, and $'$ is for differentiation as a function of pressure. The coefficients have been evaluated in Eq. **10** such that P_S and ΔE_S both vanish as f goes to zero. The resulting P–V equation of state (Birch–Murnaghan form) is

$$P_S = 3K_{0S}f(1 + 2f)^{5/2}[1 + (3/2)(K'_{0S} - 4)f + \ldots]. \quad [11]$$

Combining Eq. **9** with Eq. **6** yields

$$P_H = \{P_S + (\gamma/V_H)[(P_1(V_1 - V_H)/2 + \int_{V_1}^{V_H} P_S dV \{1-(\gamma/V_H)(V_1-V_H)/2\}^{-1} \quad [12]$$

with $P_1 = P_1(V_1)$ being the precompression pressure at volume V_1, and $P_H = P_H(V_H)$ and $P_S = P_S(V_H)$ are the Hugoniot and isentrope pressures at volume V_H. Here, we ignore the possibility of phase transformations to avoid complicating the discussion, but such transformations (e.g., solid–solid, or melting) can be taken into account if the equation of state and initial energy of the high-pressure phase is known. Applying Eqs. **10** and **11** to Eq. **12**, the Hugoniot pressure normalized by the zero-pressure isentropic bulk modulus is

$$\frac{P_H}{K_{0S}} = \{A + B + C\}\left\{1 - \frac{\gamma}{2}\left[\left(\frac{1 + 2f_H}{1 + 2f_1}\right)^{3/2} - 1\right]\right\}^{-1} \quad [13a]$$

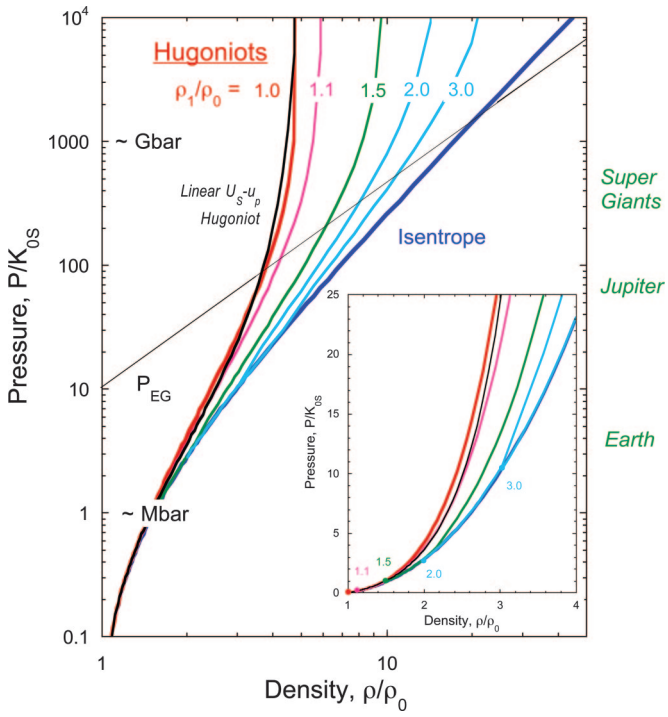

Fig. 5. Predicted pressure–density equations of state for condensed matter, caused by isentropic compression (isentrope: heavy dark blue curve), shock compression (Hugoniot: heavy red curve, $\rho_1/\rho_0 = 1.0$), and shock compression of samples precompressed to initial densities of $\rho_1/\rho_0 = 1.1$, 1.5, 2.0, and 3.0 (thin red, green, turquoise, and blue curves, respectively) assuming $K'_{0S} = 4$, $\gamma_0 = 1.5$, and $\gamma_e = 0.2$ (see text). Pressure and density are normalized to the zero-pressure bulk modulus and density, respectively, and the Mbar (= 100 GPa) and Gbar (= 100 TPa) pressure regimes are indicated based on a typical value of $K_{0S} \approx 10^{11}$ Pa; corresponding central pressures for Earth, Jupiter, and supergiant planets are indicated on the right. The Hugoniot for the linear $U_S - u_p$ relation (Eq. **7**) and the density dependence of the electron–gas pressure, $P_{EG} \approx \rho^{5/3}$ (ref. 9; only the slope, not the absolute value, has meaning here) are shown by thin black and gray lines. Because c in Eq. **7** is the zero-pressure bulk sound velocity, $(K_{0S}/\rho_0)^{1/2}$, its value is absorbed in our pressure normalization; in accord with $K'_{0S} = 4$ for the finite-strain calculations, we set $s = 5/4$ (17). Conditions near zero pressure are shown on a linear plot (*Inset*) to complement the log–log plot of the main figure.

$$A = 3(1 + 2f_H)^{3/2}f_H\{1 + [2 + (3/2)(K'_{0S} - 4 - \gamma)]f_H + 3(K'_{0S} - 4)[1 - (\gamma/2)]f_H^2 + \ldots\} \quad [13b]$$

$$B = 9(\gamma/2)(1 + 2f_H)^{3/2}f_1^2[1 + (K'_{0S} - 4)f_1 + \ldots] \quad [13c]$$

$$C = 3(\gamma/2)(1 + 2f_1)f_1[(1 + 2f_H)^{3/2} - (1 + 2f_1)^{3/2}] \cdot [1 + (3/2)(K'_{0S} - 4)f_1 + \ldots]. \quad [13d]$$

Without precompression, $f_1 = 0$; consequently, the terms B and C vanish and the denominator in Eq. **13a** is simplified.

To focus on general scaling relations, rather than detailed calculations for specific materials, we assume $K'_{0S} = 4$ *(second order or Birch equation of state),* $\gamma/V = \gamma_0/V_0 =$ constant and $\gamma_0 = 1.5$ because these are typical values for condensed matter ($K'_{0S} \approx$ 3–6 and $\gamma_0 \approx$ 1–2 in many instances) (17). In addition, we add an electronic component to the Grüneisen parameter, $\gamma_e = 0.2$, to account for excitation of electrons when the thermal energy exceeds $[E_H(V) - E_S(V)]/K_{0S}V_0 > 0.1$, and treat the precompression as being isentropic rather than isothermal, ignoring the approximately percent-level difference between the isotherm and isentrope pressure at volume V_1. The results show that Gbar (= 100 TPa) pressures are expected for materials com-

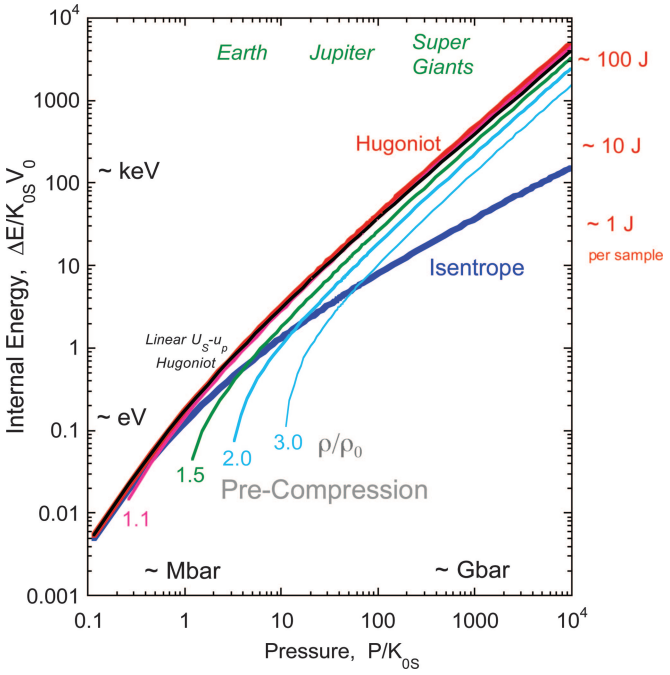

Fig. 6. Internal energy as a function of pressure corresponding to Fig. 5, showing the isentrope and the Hugoniots for initially uncompressed (red) and precompressed samples (thin red, green, light blue). Approximate dimensional values for the axes are indicated assuming $V_0 \approx 5$ cm^3 per mol of atoms and $K_{0S} = 10^{11}$ Pa; a typical precompressed sample size is ≈400 μm diameter by 10 μm thick, or ≈300 nmol of atoms. Note that the pressure dependence of the Hugoniot energy for the linear $U_S - u_p$ relation (Eq. **7**) (black) is similar to that derived from the Mie–Grüneisen analysis (Eq. **9**).

pressed ≈4- to 20-fold (in ρ/ρ_0) for the Hugoniot and isentrope, respectively (Fig. 5). Detailed pressures would differ for different parameter values than those assumed here (larger values of γ increase the Hugoniot pressure at a given volume, and larger values of K'_{0S} increase both the adbiabat and Hugoniot pressure at a given volume). Also, more terms may be needed in the finite-strain expansions (Eqs. **10**, **11**, and **13**) at high compressions; and the linear $U_S - u_p$ relation (Eq. **7**) yields an infinite Hugoniot pressure at a density $\rho/\rho_0 = s/(s-1) = 5$ for the value of s used here (8, 16).

The effect of precompression is to significantly decrease the thermal pressure of the Hugoniot state, with much of the P–ρ regime between the Hugoniot and isentrope (or isotherm) being accessible with as little as 50% (1.5-fold) initial precompression (Fig. 5). Thus precompression is closely analogous to the application of multiple shocks, including in the fact that breaking a shock front into as few as four reverberations makes the compression nearly isentropic (22). As compressible fluids of planetary interest, such as H_2 and He, can be subjected to relatively large precompressions, it is evident that the high-pressure thermodynamic state can be effectively tuned over a broad range of temperatures or internal energies (Fig. 6).

Megajoule-class lasers represent the state of the art in facilities currently under development for laser-shock experiments (23). As these consist of ≈10^2 beams, each delivering 1–10 kJ, Fig. 6 suggests that energies corresponding to Gbar pressures should be deliverable to a precompressed sample even if only a fraction of the beams can be used with limited efficiency (e.g., 10 1-kJ beams coupled at 1% efficiency to provide 100 J in the sample). Thus, Gbar pressures with tunable final thermal states will become accessible in the laboratory.

One of the key benefits of the high energy-density laser facilities is not only that they deliver pulses having high power

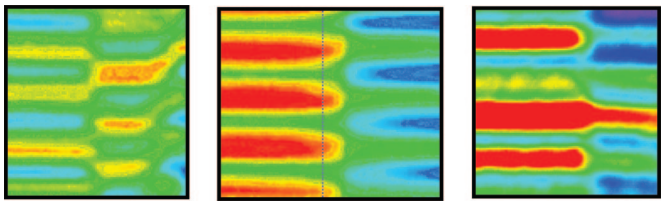

Fig. 7. VISAR records of shock-loaded H_2O (precompressed to ≈1 GPa) showing the transition from transparent behavior at $P \approx 50$ GPa and $T < 3{,}500$ K (*Left*: reflection of diamond-sample interface is visible through the shock-compressed sample, before and after first breakout); to opaque at $P \approx 100$ GPa and $3{,}500 < T < 9{,}000$ K (*Center*: reflection disappears on breakout); to reflecting at $P > 150$ GPa and $T > 9{,}000$ K (*Right*: new reflection appears from shock front, as evident from time-dependent (curved) fringes after breakout) (14). Time and distance across the sample are along the horizontal and vertical axes, respectively, and red (vs. blue) colors indicate higher recorded intensity of light.

(≈PW/cm^2) over the 0.5- to 1-mm width of the sample area, but also that they can do so for the relatively long period of ≈10–20 ns (versus the τ ≈1- to 4-ns effective pulse width of current facilities) (23). This capability is directly relevant to our experiments, because the shock front is followed by a rarefaction wave that develops at the end of the laser pulse (i.e., at time τ) and catches up with the shock in a time interval Δt from the initiation of shock loading. The shock wave thus travels a distance $U_S\,\Delta t$ before being attenuated. The rarefaction, which starts after the interface has traveled a distance $u_p\tau$, travels at approximately the velocity $U_S + u_p$ because the material is moving at velocity u_p and the local (high-pressure) sound velocity is about equal to the shock velocity. Therefore, the catch-up distance is

$$\Delta x = U_S \Delta t \approx (U_S + u_p)(\Delta t - \tau) + u_p \tau \qquad [14]$$

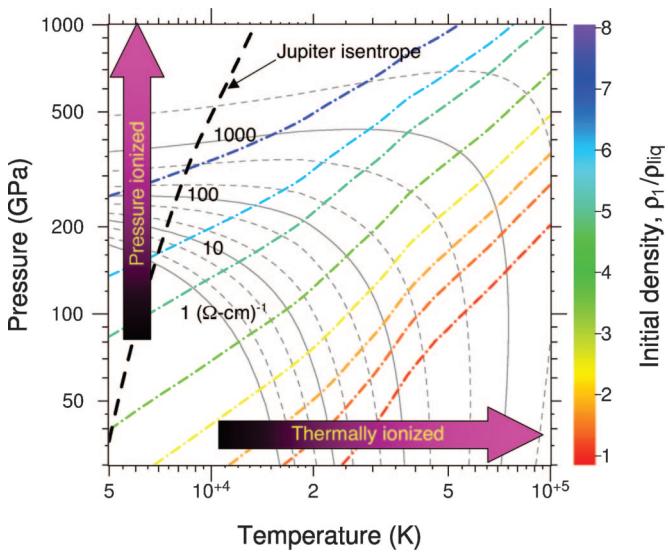

Fig. 8. Predicted contours of electrical conductivity (thin gray solid and dashed curves) for He as a function of pressure and temperature, showing that metallic properties can be induced either by high P or high T. These influences can be separately documented by varying the initial density of the sample: colored dot-dash curves trending from lower left toward upper right indicate Hugoniots for different degrees of precompression (1- to 7-fold initial compression, as indicated by the color scale). Electrical conductivity can be experimentally inferred from optical absorption and reflectivity (see Fig. 7), and the contours shown here are based on thermodynamic and semiconductor models (24–26). A model isentrope for Jupiter's interior is shown for comparison (dashed black curve).

such that

$$\Delta x \approx U_S^2 \tau / u_p \sim (10^2\ \mu\text{m/ns})\,\tau. \quad [15]$$

As a result, a 10- to 20-ns pulse width allows use of an ≈1-mm-thick diamond on the entry side, typical of the anvils that are used in static-compression experiments at Mbar pressures. Rather than being limited to the 1- to 5-GPa pressures, as at present, precompressions to the 100-GPa range should thus be possible in experiments at the largest laser facilities now under development (e.g., a millimeter-diameter laser-generated shock front generated at the surface of a 0.8-mm-thick diamond anvil avoids side rarefaction). That is, samples already transformed to a high-pressure, for example, metallic, state could serve as starting materials for experiments to the 10- to 100-TPa level.

Initial Experiments and Future Potential

Fig. 7 illustrates the potential of laser-shock experiments on precompressed materials. Here, VISAR is used to characterize the optical properties of the sample and determine the Hugoniot pressure and density. In addition, an estimate of the blackbody temperature of the sample is obtained by optical pyrometry. The experiments clearly show that H_2O transforms from a transparent dielectric at low pressures and temperatures (light visible even after transmission through the shock-compressed region) to a metallic-like state (light reflected off the shock front) when taken to pressures and temperatures exceeding 100–150 GPa and 6,000–9,000 K (14). The profound change in outer, valence-electron states (i.e., in chemical bonding) induced by high pressures and temperatures is visibly evident.

It is crucial that pressure and temperature can be separately tuned because either can induce electronic changes in materials. Helium, for instance, can be either thermally ionized or pressure-ionized, and it is by varying the initial compression that one can experimentally validate theoretical expectations of the conditions under which the insulator–metal transition takes place (Fig. 8). The effect of ionization is to increase the pressure at a given density, and this is handled by including an explicit temperature dependence to the Grüneisen parameter. To the degree that electrons are thermally ionized, the thermal pressure intrinsically becomes a function of temperature (or thermal energy) and, along with other pressure-induced (e.g., structural) phase transitions, this influences the equation of state. A major incentive for precompressing samples is to be able to vary such high-temperature phenomena, so as to be able to experimentally distinguish them from the effects of compression alone.

These results, illustrating dramatic changes in chemical bonding at Mbar (100 GPa) conditions, reinforce the significance of being able to achieve significantly higher pressures in the future (Figs. 5 and 6). Evidently, compressional-energy changes can reach keV in the Gbar (100 TPa) regime, comparable to energies of core-electron orbitals. Deep-electron levels within the atom can therefore participate in chemical bonding, and an entirely new type of chemistry becomes accessible in a (subnuclear) regime that is as yet unexplored by experiments.

We thank R. Cauble, B. K. Godwal, L. R. Benedetti, D. G. Hicks, S. Morris, and D. Spaulding for helpful discussions and comments. This work was supported by the U.S. Department of Energy and National Science Foundation.

1. Vladimirov AS, Voloshin NP, Nogin VN, Petrovtsev AV, Simonenko VA (1984) *Sov Phys JETP Lett* 39:85–88.
2. Cauble R, Phillion DW, Hoover TA, Kilkenny JD, Lee RW (1993) *Phys Rev Lett* 70:2102–2105.
3. Trunin RF (1998) *Shock Compression of Condensed Materials* (Cambridge Univ Press, Cambridge, UK).
4. Eremets MI (1996) *High Pressure Experimental Methods* (Oxford Univ Press, Oxford).
5. Jeanloz R (1989) *Annu Rev Phys Chem* 40:237–259.
6. Hemley RJ, Ashcroft NW (1998) *Phys Today* 51:26–32.
7. Butler RP, Wright JT, Marcy GW, Fischer DA, Vogt SS, Tinney CG, Jones HRA, Carter BD, Johnson JA, McCarthy C, Penny AJ (2006) *Astrophys J* 646:505–522.
8. Zel'dovich YB, Raizer YP (2002) *Physics of Shock Waves and High-Temperature Hydrodynamic Phenomena* (Dover, Mineola, NY).
9. Eliezer S, Ghatak A, Hora H (2002) *Fundamentals of Equations of State* (World Scientific, Singapore).
10. Lee KKM, Benedetti LR, Mackinnon A, Hicks D, Moon SJ, Loubeyre P, Occelli F, Dewaele A, Collins GW, Jeanloz R (2002) in *Shock Compression of Condensed Matter*, ed Furnish MD, Thadhani NN, Horie Y (American Institute of Physics, Melville, NY), pp 1363–1366.
11. Loubeyre P, Celliers PM, Hicks DG, Henry E, Dawaele A, Pasley J, Eggert J, Koenig M, Occelli F, Lee KKM, *et al.* (2004) *High-Pressure Res* 24:25–31.
12. Mao HK, Bell PM, Shaner JW, Steinberg DJ (1978) *J Appl Phys* 49:3276–3283.
13. Marsh SP (1980) *LASL Shock Hugoniot Data* (Univ California Press, Berkeley, CA).
14. Lee KKM, Benedetti LR, Jeanloz R, Celliers PM, Eggert JH, Hicks DG, Moon SJ, Mackinnon A, Da Silva LB, Bradley DK, *et al.* (2006) *J Chem Phys* 125:014701.
15. Celliers PM, Bradley DK, Collins GW, Hicks DG, Boehly TR, Armstrong WJ (2004) *Rev Sci Instrum* 75:4916–4929.
16. McQueen RG, Marsh SP, Taylor JW, Fritz JN, Carter WJ (1970) in *High Velocity Impact Phenomena*, ed Kinslow R (Academic, San Diego), pp. 294–419.
17. Jeanloz R (1989) *J Geophys Res* 94:5873–5886.
18. Fabbro R, Fournier J, Ballard P, Devaux D, Virmont J (1990) *J Appl Phys* 68:775–784.
19. Lindl JD, Amendt P, Berger RL, Glendinning SL, Glenzer SH, Haan SW, Kauffman RL, Landen OL, Suter LJ (2004) *Phys Plasmas* 11:339–491.
20. Holzapfel GA (2000) *Nonlinear Solid Mechanics: A Continuum Approach for Engineering* (Wiley, New York).
21. Birch F (1978) *J Geophys Res* 83:1257–1268.
22. Lyzenga GA, Ahrens TJ (1982) *Am Instit Phys Conf Proc* 78:231–235.
23. National Research Council (2003) *Frontiers in High Energy Density Physics* (Natl Acad Press, Washington, DC).
24. Forster A, Kahlbaum T, Ebeling W (1992) *Laser Part Beams* 10:253–262.
25. Hicks DG, Celliers PM, Collins RW, Eggert JH, Moon SJ (2003) *Phys Rev Lett* 91:035502.
26. Celliers PM, Collins GW, Hicks DG, Koenig M, Henry E, Benuzzi-Monaix A, Batani D, Bradley DK, DaSilva LB, Wallace RJ, *et al.* (2004) *Phys Plasmas* 11:L41–L44.